Influence of powder characteristics on the microstructure and mechanical properties of HIPped CM247LC Ni superalloy

MacDonald, J. E.; Khan, R. H.U.; Aristizabal, M.; Essa, K. E.A.; Lunt, M. J.; Attallah, M. M.

DOI:
10.1016/j.matdes.2019.107796

Influence of Powder Characteristics on the Microstructure and Mechanical Properties of HIPped CM247LC Ni Superalloy

JE MacDonald[a], RHU Khan[a], M Aristizabal[a], KEA Essa[a], MJ Lunt[b], MM Attallah[a]

[a] *School of Metallurgy and Materials, University of Birmingham, Birmingham, B15 2TT, UK*

[b] *DSTL, Salisbury, Wiltshire, SP4 0JQ, UK*

ABSTRACT

This work investigates the influence of gas atomised powder particle size and characteristics on the microstructure and mechanical properties of hot isostatically pressed (HIPped) CM247LC nickel-base superalloy powders. Three different GA powders (particle size ranges: 53-150 μm; 0-150 μm; 15-53 μm) of very similar compositions were HIPped at the γ′ solvus temperature. Microstructural analysis and tensile testing were conducted on as-HIPped samples. It was found that the fine powders promote the formation of prior particle boundaries (PPBs) decorated with carbide and oxy-carbide clusters due to the higher oxygen content per weight in fine powders, which adversely affects the mechanical properties. It was also found that coarse powder particles are beneficial for minimising PPBs and increasing the twin boundaries fraction. Nonetheless, the best balance of high temperature tensile properties was in the wide range powder (0-150 μm). The effect of particle size was further investigated by sieving the wide range powder into two particle size distributions. Tensile testing of these conditions showed that the hot ductility could be further improved by removing the very fine powder particles. Both of the sieved powders exhibited better hot ductility than the wide range powder and also outperformed the 53-150 μm and 15-53 μm powders.

Keywords: Ni-superalloys; powder hot isostatic pressing; microstructure; mechanical properties.

1. Introduction

Powder hot isostatic pressing (HIPping) of Ni-superalloys has the potential to yield superior components with improved buy-to-fly ratio over traditional processing routes [1-4]. There are, however, a number of issues with the powder HIPping of superalloys that need to be addressed, before the netshape advantages can benefit production of critical high temperature aero-engine components, such as combustor and turbine casings. From a microstructural

perspective the main issue is the presence of a significant density of oxides, carbides, and oxy-carbo-nitrides, forming prior particle boundaries (PPBs). PPBs are particularly detrimental to the mechanical properties, as they form continuous networks throughout the microstructure, ultimately leading to particle de-bonding and void formation during high temperature deformation [5-8]. Their presence can also complicate microstructural control during post-HIPping heat treatment by hindering grain coarsening [9]. Another less common issue is that brittle ceramic oxide phases (e.g. ZrO_2, Al_2O_3 and TiO_2) can be present owing to inclusions from the atomisation process or the O-rich layer on the powder particle surfaces. Such surface oxides may act as nuclei for the formation of primary MC carbides at the PPBs [5], which can occur even when the carbon (C) content is very low (<0.02 wt.%) if sufficient oxygen is present [5, 6]. These phases on powder particle surfaces can serve as crack initiation sites. Minimising O and C levels, the addition of stable carbide formers (e.g. Hf & Ta) [10, 11], increasing the HIPping temperature to promote grain growth past PPBs [8, 11], and heat treatment (hot outgassing) of powder before consolidation [3, 12] are all methods that have been reported to reduce PPB precipitation in as-HIPped superalloy components.

CM247LC (where LC stands for low carbon) is a Ni superalloy with a potential for operation at high temperatures (≈750°C) due to the high γ′ volume fraction (V_f). This alloy also has a moderate Cr level, which help prevent the formation of brittle topologically close packed (TCP) phases under long holds at high temperature [13-15]. Property data is available for cast and directionally solidified CM247LC [16-18] however limited data is available for HIPped CM247LC. In the present work, the effect of powder particle size and its influence on microstructure and tensile properties of the as-HIPped CM247LC has been studied.

2. Experimental procedure

Three argon gas atomised (GA) CM247LC powders with similar compositions were selected for investigation. The powders had particle size ranges of 53-150 μm, 0-150 μm and 15-53 μm, which were designated as ‘coarse’ (C) (Sandvik Osprey), ‘wide range’ (WR) (Carpenter Powder Products), and ‘fine’ (F) (LPW technology Ltd.), respectively. The chemical composition of the powder is shown in table 1, measured using Inductively Coupled Plasma (ICP) (the main alloying additions), Combustion (C+S), and Fusion (N + O). Since the testing equipment was not sensitive enough to measure O levels below 100ppm, the supplier’s data for O content is also included. The low C content and the moderate levels of Hf and Ta should be suited to minimising PPB precipitation during HIPping.

Table 1: Composition (wt.%) of CM247LC powders investigated.

	C	Al	Ti	Cr	Mo	Hf	Ta	Co	W	B	N	O	O (supplier)	Ni
C	0.08	5.55	0.71	8.34	0.52	1.23	3.11	8.73	9.34	20ppm	<20ppm	<100ppm	20ppm	Bal.
WR	0.09	5.57	0.80	8.29	0.61	1.31	3.10	9.59	9.57	140ppm	<20ppm	<100ppm	75ppm	Bal.
F	0.07	5.60	0.78	8.07	0.51	1.35	3.23	8.75	10.0	140ppm	<20ppm	120ppm	120ppm	Bal.

The powder morphology, internal defects and HIPped microstructures were analysed using a Philips XL-30 SEM linked with energy dispersive X-ray spectroscopy (EDX) and a JEOL 7000 FEG-SEM microscope. Image analysis was conducted with ImageJ software for quantitative analysis of γ′ volume fraction (V_f), measuring at least 1000 particles for each analysis. Powder flow rate, apparent density (AD_H) and tap density (ρ_T) were measured as per the ASTM standards listed in table 2 using a Hall's flowmeter. The particle size distribution (PSD) was measured using sieve analysis. Differential scanning calorimetry (DSC) was conducted on the as-received powders using a DSC 404 C Pegasus® machine to assess the phase changes from 900-1450°C heated at 10˚C/min. to 1450˚C and subsequently cooled at 10˚C/min.

The powder was encapsulated in mild steel canisters, degassed for 48 hours, crimped and welded to seal-off under a vacuum of $<10^{-5}$ mbar. The canisters were consolidated in an EPSI HIPping system equipped with a Mo-furnace and type-B thermocouples for temperature control and measurement. HIPping was performed at 1260°C, 150 MPa pressure using a 2 h dwell time, and heating and cooling rates of 5°C·min^{-1} to/from the dwell temperature. These parameters were investigated in previous work by Zhang [11], where HIPping at the γ′ solvus temperature gave the best balance of elevated temperature (ET) properties. The HIPped samples were sectioned and examined under the SEM. EDX was conducted on as-polished samples, whilst others were etched with Kalling's no. 2 reagent or electrochemically etched using 10% phosphoric acid (H_3PO_4) solution in H_2O under 4V for 10sec, to further reveal the microstructure, especially the γ′ phase. Electron back-scattered diffraction (EBSD) was conducted on the XL-30 SEM and the data was analysed using HKL Channel 5 software. Grain maps were taken at x200 magnification with a 1 µm step size and x400 magnification with a 0.75 µm step size to characterise the grain size and structure. ET tensile tests were conducted at 750°C (per ASTM E8). The fracture surfaces were analysed under the SEM.

The powder yielding the best balance of ET tensile properties (wide range as it will be discussed) was further sieved into two other PSD, which are designated as 'sieved coarse' (S_c: 53-150 µm) and 'sieved fine' (S_f: 25-53 µm), effectively cutting off the <25µm powders tail. Each of these sieved powders were HIPped with identical parameters to those used previously. EBSD allowed analysis of the grain structure and ET tensile testing was conducted at 750°C.

3. Results & Discussion

3.1 Powder characterisation

The chemical compositions of the powders were almost identical (table 1), except that the coarse powder had a lower B content, the wide range powder had a slightly higher Co content, whilst the fine powder gave the highest O content. A near spherical particle morphology (figure 1) was common with all powders. Typical GA microstructural features such as the presence of satellite particles and a fine dendritic structure on the surface of powder particles can be seen in figure 1(a-c).

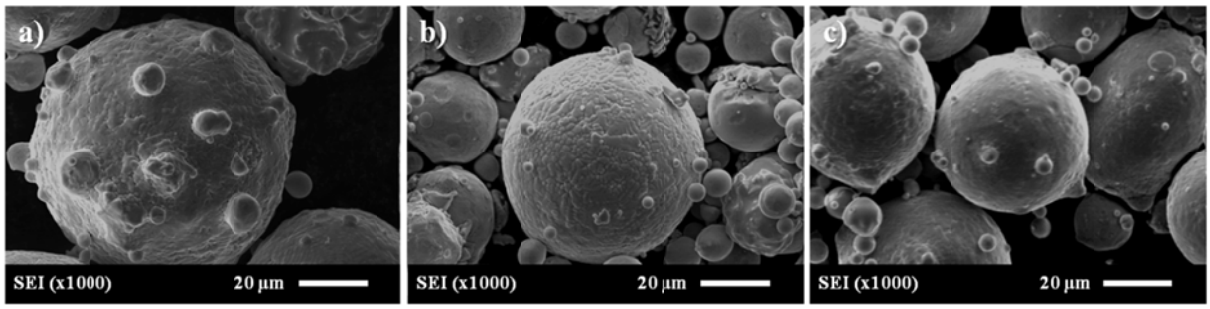

Figure 1: SEI-SEM powder particle morphology images showing mainly spherical morphology, dendritic structure on surfaces and satellite particles: (a) Coarse; (b) Wide range; (c) Fine powder.

Figure 2 shows the PSDs of the powders measured by sieve analysis. All the powders are considered to be uni-modal. The wide range powder exhibited a slight peak in the 20-45 µm range as well as the 53-63 µm range, but insignificant enough to be considered bi-modal. The physical properties of the powders are shown in table 2. The packing density was calculated by taking the tap density as a percentage of the theoretical density for CM247LC – 8.50g·cm^{-3} reported by Harris *et al.* [19]). The three powders were fairly similar although the wide range powder had a slightly lower flowability but a better packing density due to the combination of fine and coarse powder particles. In powder HIPping, a good flowability is desirable for

canister filling whilst good packing density minimises shrinkage, which makes canister design less sophisticated. The fine (S_F) powder had a poor flowability, as it did not flow through the Hall's flowmeter.

DSC thermal analysis was used to evaluate the phase transformation temperatures of the CM247LC powders (e.g. γ′ solvus, incipient melting, etc…) to identify the HIPping temperature window. The three powder conditions gave similar DSC traces, similar to the one in Figure 3 from the wide range powder. Melting occurred in the range 1310~1390°C. The austenite (γ) phase (as reported in [20] for cast CM247 material) formed around 1365°C. There were no obvious peaks for carbide formation due to the low carbon content. Another slight exothermic peak was observed on cooling around 1260°C, which was attributed to the formation of γ′ and this was selected as the HIP temperature to allow sufficient grain growth and to potentially eliminate PPB networks. A more pronounced γ′ peak was not observed due to the high cooling rates during the powder atomisation process. The slight difference in $T_{liquidus}$ between the heating and cooling segments of the DSC trace is probably due to the transformation of the powder material into liquid, prior to superheating to 1450˚C, followed by cooling. Limited temperature differences (±10˚C) were seen between the three powders sizes, especially for the melting range. No differences were seen however in the DSC traces of the HIPped material.

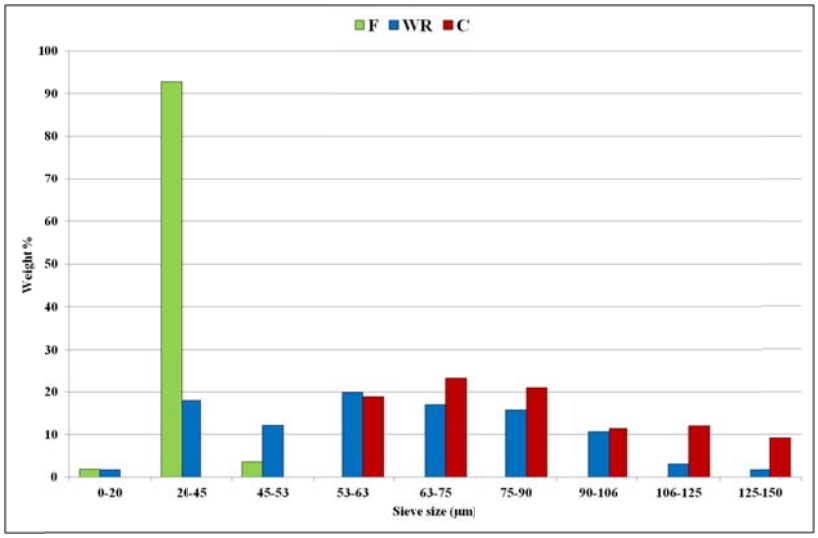

Figure 2: Particle size distribution (PSD) for the CM247LC powders investigated.

Table 2: Properties of the CM247LC powders.

Powder	Flow rate (s)	AD_H (g/cm^3)	ρ_T (g/cm^3)	Packing density (%)
C	14	4.6	5.4	63
WR	15	4.8	5.8	68
F	14	4.5	5.3	62
S_C	15	4.45	5.17	60.5
S_F	/	4.47	5.29	62
ASTM Standard	B213-13	B212-09	B527-06	/

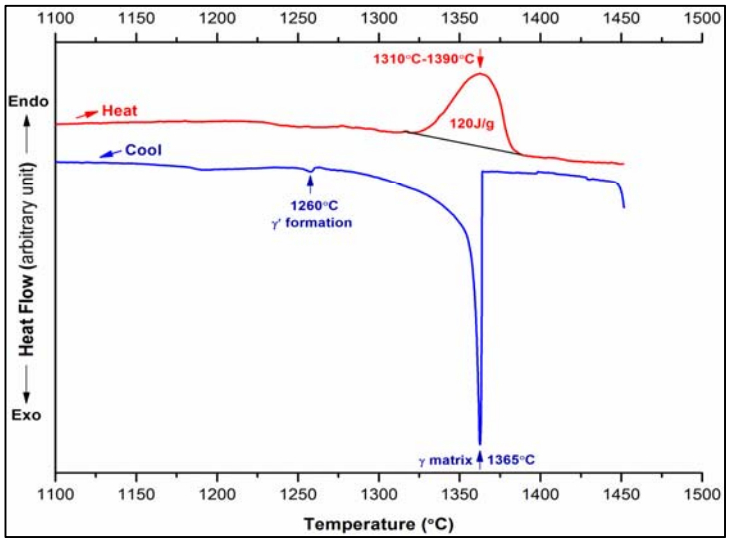

Figure 3: A DSC trace for the phase transformations in CM247LC wide range powder, showing the melting range and the formation temperatures for the γ and γ′ phases.

ThermoCalc analysis results are also included to assess the fraction of different phases as a function of temperature, using the TCNI5 database. The phase transformation temperatures are shown in table 3, which gives a comparison of the modelling and the experimental data. The transition temperatures suggested by the modelling are relatively lower than those given using the DSC for powders. This highlights the importance of conducting thermal analysis on different batches of powder since the γ′ solvus temperature is a critical processing temperature in powder HIPping.

Table 3: Comparison of the phase transformation temperatures for CM247LC.

	Phase transition temperatures (°C)	
	DSC	ThermoCalc
γ formation ($T_{Liquidus}$)	1365 **(cooling)**	1330
γ′ solvus	1260	1245

3.2 As-HIPped Microstructure

3.2.1 Chemical composition

The chemical composition of the HIPped material was generally similar to the powder with the exception that O-content invariably increased in the as-HIPped samples, with the coarse and wide range powders HIPped material achieving 120 ppm and 140 ppm, respectively. The fine powder exhibited a larger increase in O content from 120 to 240 ppm. O pick-up in powder HIPping occurs despite degassing as the HIPped components could 'pick-up' residual O from the canister/atmosphere. The larger increase with the fine powder is due to the increased surface area to volume ratio.

3.2.2 Gamma prime (γ') phase

As-HIPped CM247LC had a γ′ V_f of 62% and all HIPped powders exhibited a 'necklace' structure, consisting of fine γ′ within the grains and coarse γ′ decorating the grain boundaries. An example of this is shown in Figure 4(a), where coarse γ′ particles can be seen around the edges of the grains (which have irregular boundary morphologies) whilst fine γ′ populates the grain interiors (figure 4b). This necklace structure was also consistent with microstructures obtained by Zhang, [11] (where 0-60 μm powder was used) and has been reported elsewhere [22] as a stable state for Ni-base superalloys. The fine γ′ was around 1 μm in size, with cuboidal array type morphology (coarsened 'split-cube' particles with irregular shaped edges) that distributed homogeneously within the grains. Both the coarse grain boundary γ′ and the ~1 μm split-cube γ′ are considered to be primary and secondary γ′, respectively, according to the size definitions as reported by Jackson and Reed [23]. In the channels between the split-cube particles, ultra-fine tertiary γ′ particles, as shown in Figure 4c, were observed (although these particles were not included in the quantitative analysis of γ′ V_f). The phases present were similar from all three powders so only one image for each type has been included in Figure 4.

3.2.3 Other phases

EDX analysis was conducted on the other phases that can be seen in Figure 5. The finer type of the particles with brighter contrast were found typically to be rich in Ta, Hf, C and sometimes O suggesting they are (Hf, Ta)C carbides or oxy-carbides. Sometimes O was detected in such particles, which could be due to Hf + Ta 'gettering' oxygen from the matrix. The larger type of phase, identified as HfO_2 by EDX analysis was also observed in all microstructures, although it appeared more common with the coarse powder, where some

very large, irregular HfO_2 phases were found. Table 4 gives typical EDX results for these types of carbides and Hf-containing inclusions. The HfO_2 particles/clusters varied significantly in size and morphology as shown in Figure 5. Such inclusions can originate from the atomisation process, as mentioned in section 1, although the coarse powder particles are thought to be worse since they may gather coarser inclusions. However, the wide range powder also contained coarse particles, but such large inclusions were not found with that powder, which highlights one of the issues of GA powder production in that there can be significant variation from one atomiser to another.

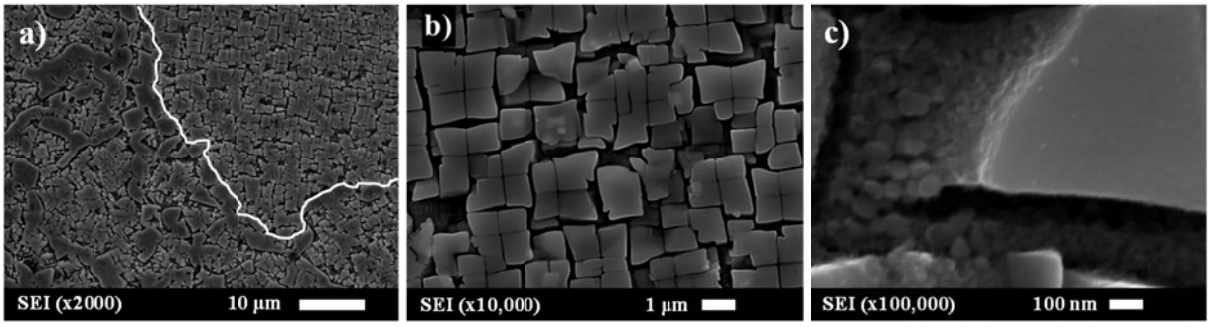

Figure 4: SEI-SEM micrographs showing the phases present in the as-HIPped CM247LC: (a) Necklace structure of coarse γ′ at grain boundaries (outlined in white for the large grain at the top right of the image) with fine γ′ in the grain interior, (b) high magnification image of the fine (1 µm) γ′ with irregular cuboidal morphology, and (c) ultra-fine tertiary γ′.

Table 4: EDX analysis of the various particles in HIPped CM247LC in Figure 5, suggesting the fine particles were (Hf, Ta) carbides and the inclusions were HfO_2 (wt%).

	Al	Ti	Cr	Co	Mo	Hf	Ta	W	O	Ni
Carbide	2.80	1.23	5.33	5.67	0.33	23.01	22.44	4.17	-	35.02
Inclusion	1.57	0.20	2.13	1.83	0.07	74.57	2.03	0.54	3.77	13.31

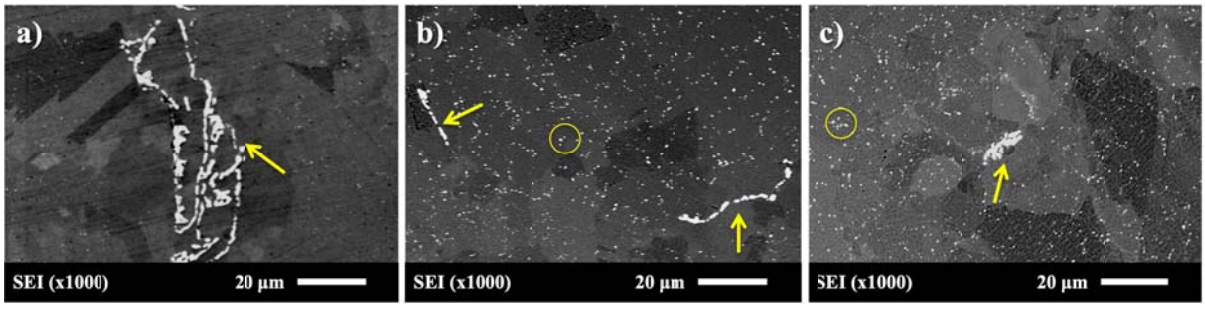

Figure 5: SEI-SEM micrographs of the Hf+O rich inclusions (arrowed) and (Hf,Ta)-rich fine particles (circled), showing (a) large and irregular particles/clusters sometimes found within

the coarse powder, (b) similar, but generally finer clusters in the wide range powder, and (c) localised clusters in the fine powder. The chemical analysis of the different particles is given in Table 4.

3.2.4 – Prior Particle Boundaries (PPBs)

HIPping at 1260°C generally promoted sufficient growth for grains to pass PPBs, leaving carbides distributed within grains and along the grain boundaries. Continuous PPB networks were often difficult to find, although there were differences in PPB decoration between the different powder batches as shown in figure 6. Coarse powder particles promoted grain growth past PPBs, giving a dispersed distribution of carbides, Figure 6(a). The lower O content of the coarse powder contributed to PPBs/carbide rings being difficult to distinguish throughout the microstructure; and where they could be recognised, they were isolated, often incomplete and only very faintly decorated with fine precipitates. When fine powder particles were present however, grain growth did not always occur through the PPBs, which were found more frequently in the microstructure. With the wide range powder, across the majority of the bulk material, the carbides appeared dispersedly distributed (similar to the coarse powder). However certain, regions exhibited carbide clusters and PPBs with denser decoration (Figure 6b, bottom left and righ). These tended to be regions surrounded by groups of smaller grains, believed to form by the agglomeration of a number of very fine (<15 µm) powder particles. Overall, PPB networks were pronounced in the fine powder, with the carbide rings being more frequent, Figure 6(c). They were typically more heavily decorated and occasionally conjoined to others. This effect of reduced PPB decoration with coarser powder and lower O content is consistent with investigations done on powder particle size by Rao *et al.* [6] and May *et al.* [24] on IN718 and RR1000, respectively.

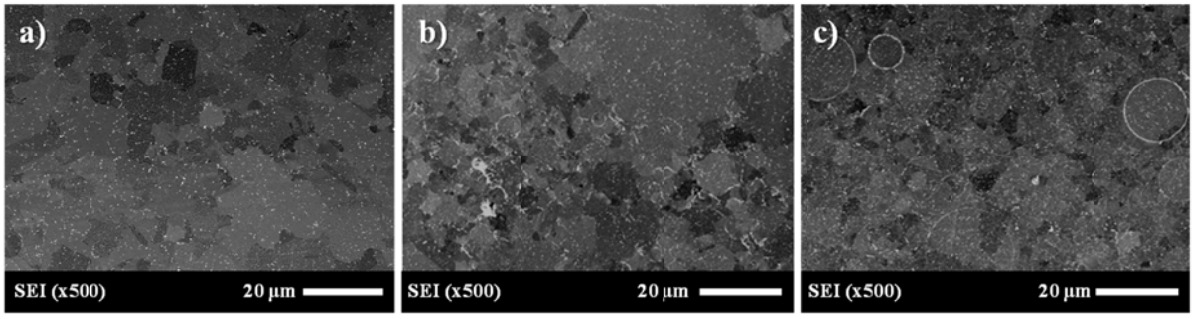

Figure 6: SEI-SEM micrographs for the PPB networks in the as-HIPped microstructures, showing (a) coarse powder: grains outgrew PPBs leaving the carbides well dispersed, (b) wide range powder: generally well dispersed carbides with occasional carbide clusters due to

the agglomeration of fine particles, and (c) fine powder: clear carbide rings can be seen at PPBs though grain growth occasionally occurred past the PPBs.

3.2.5 Grain size & structure

The low O-content in the coarse powder particles promoted grain growth past the limited PPBs, which led to a relatively coarse grain structure. The wide range powder contained both relatively coarse and fine powder particles, which lead to a more bi-modal grain distribution whereas the grain size was fine and more consistent with the fine powder. EBSD analysis (table 5) showed that the average grain sizes were around 21 μm, 18 μm and 12 μm from the coarse, wide range and fine powders, respectively. Grain boundaries often had irregular morphologies with all powders, which may be in part due to pinning of grain boundaries by the coarse γ′ particles of the necklace structure or the fine carbides. The development of significant grain boundary serrations has been reported with RR1000 by Mitchell *et al.* [25], by controlling the cooling rate from above the γ′-solvus, with the presence of γ′ particles pinning the grain boundaries. It may be possible to increase the serrations in the as-HIPped CM247LC with closer control of the HIPping temperature and cooling rate. Such serrations have been found to significantly improve the stress-rupture properties of Ni-superalloys [25-29].

A number of straight grain boundaries such as in figure 7, were also observed under SEM, suggesting the formation of annealing twins, which varied depending on the powder. They were observed more frequently within the coarse powder, which may be attributed to a combination of the powder particle size as well as the nominal oxygen content of the powders. Similar findings were reported by Rao *et al.* [6] in an investigation on HIPped IN718, where twinning was limited when powder had high O content. Twins can form during recrystallisation annealing following plastic deformation [6]. The application of plastic deformation at high temperature during HIPping can lead to the formation of twinning during recrystallisation. The lower degree of twinning observed in the fine powder condition may be due to the presence of more PPBs decorated with stable oxides and MC carbides, which can impede recrystallisation (as evident by the finer grain structure as well), eventually limiting the formation of annealing twins.

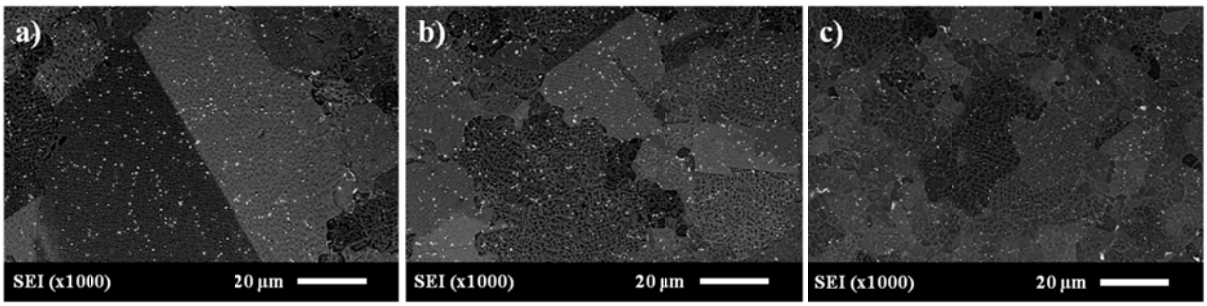

Figure 7: SEI-SEM micrographs for the twin boundaries: (a) coarse powder, (b) wide range powder, and (c) generally irregular boundary morphologies with few twins in the fine powder.

Coincidence site lattice (CSL) boundaries are special boundaries between grains with coinciding lattice points and are defined using Σ numbers, where Σ1 would denote a perfect/nearly perfect crystal. Literature on all the different types of CSL boundaries is limited but generally Σ<29 have relatively coherent interfaces containing few crystalline defects, hence are seen as beneficial. Conversely, Σ>29 boundaries tend to contain large concentrations of defects and vacancies that serve to both weaken the interface and promote diffusive mechanisms at elevated temperatures [30]. Twin boundaries in FCC materials are a special type of CSL boundary with the most coinciding lattice points, and are denoted by Σ3 [30]. EBSD was used to assess the degree of twinning and it was found that the total grain boundary length, consisting of Σ3 boundaries, varied between the powders. The coarse powder (lowest O) exhibited around 22% Σ3, the wide range powder around 12% Σ3. and the fine powder (highest O) around 10% Σ3. An example of the EBSD maps, showing band contrast with Σ3 boundaries highlighted in white, can be seen in Figure 8.

Table 5: Grain data from EBSD analysis. Generally coarse powder particles promoted the formation of coarser grains although the difference in the average grain sizes between the powder was not massive. The formation of twin boundaries also varied between powders, in general increasing as O content decreased.

	C	WR	F	S_C	WR	S_F
Mean grain ϕ (µm)	21	18	12	19	18	13
Min. ϕ (µm)	1	1	1	1	1	1
Max. ϕ (µm)	95	88	62	84	88	69
Σ3 (%)	22.4	12.2	9.7	13.6	12.2	16.6
O-Content (ppm)	120	140	240	/	140	/

For the sieved powders, EBSD grain maps can be seen in Figure 9. The S_C powder resulted in a coarse average grain size of 19 μm, although this microstructure appeared quite similar to the wide range and did not coarsen as much as the un-sieved (C) coarse powder which achieved 21 μm grain size. This may be expected since the wide range powder did not contain as high a fraction of the coarsest powder particles, as can be seen in Figure 2. The S_F powder exhibited a fine average grain size of 13 μm and a more uniform grain distribution, similar to the fine (F) powder. The differences in Σ3 boundary length between the sieved powders were not as significant as those between the other powders, although direct comparison of the powders from different suppliers is not necessarily valid due to the slight differences in chemistry (especially the O-content). The S_C powder exhibited a higher Σ3 boundary fraction (≈14%) than the WR powder as expected, attributed to the elimination of the ultra fine powder particles, which can promote the formation of carbide cluster such as those shown in Figure 6b. Thus, reducing the oxides and carbides at PPBs and allowing further recrystallisation of grains to occur. The S_F powder, however, exhibited a higher Σ3 fraction than both (≈17%), despite the lower average particle/grain size.

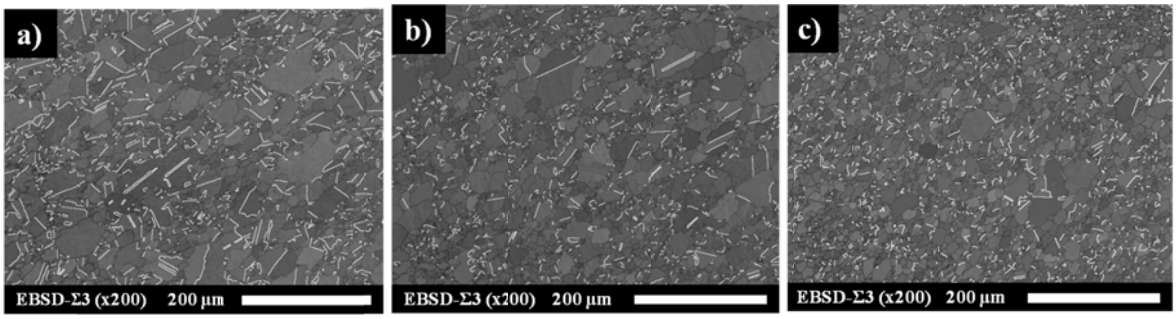

Figure 8: EBSD maps showing band contrast and Σ3 CSL twin boundaries for the (a) coarse powder, (b) wide range powder, and (c) fine powder.

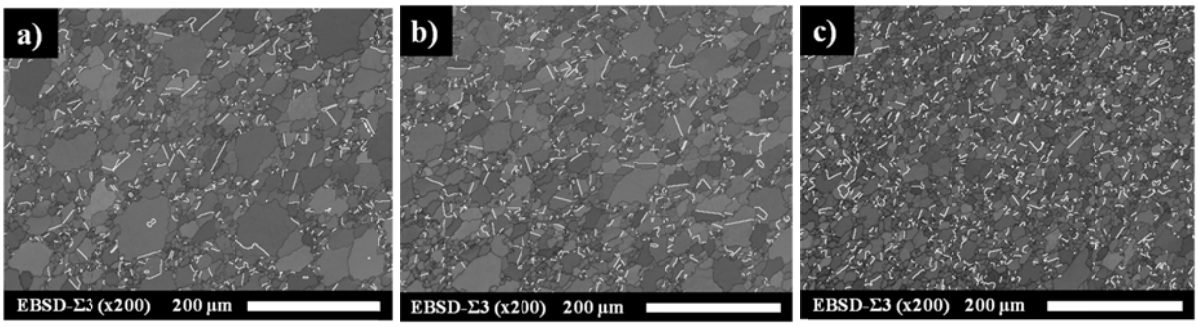

Figure 9: EBSD maps showing band contrast and Σ3 CSL twin boundaries for the (a) sieved coarse (S_C) powder, (b) wide range powder, and (c) sieved fine (S_F) powder.

Twin boundaries exhibit exceptionally low energy and have been reported to enhance creep resistance compared to a 'normal' grain boundary [30, 31]. Maximising twin boundaries may, therefore, be beneficial, although for stainless steels at least, notable improvements in properties are not achieved until microstructures exhibit around 50% Σ3 [30]. Detrois *et al.* [30] conducted a grain boundary engineering (GBE) study concerned with increasing the fraction of Σ3 boundaries via cold working and annealing, with PM RR1000. Although such secondary processing stages are unsuitable for netshape PM components, the conditions for developing these boundaries are effectively simulated during the HIP cycle. Our results show that the powder particle size may have an effect. The coarser powder particles may have promoted more plastic deformation and recrystallisation, resulting in more twinning. Finer PSDs exhibit increased PPB decoration (Figure 6), which can limit recrystallisation. Tailoring the HIP cycle to increase plastic deformation e.g. by increasing HIP temperature as investigated with IN718 [32] and 316L stainless steel [33], may also increase the CSL boundaries in the microstructure. It may, therefore, be possible to use powder HIPping as a GBE method, although further investigation would be required to see if sufficient levels could be achieved to yield significant improvements in properties. However, when considering high temperature Ni-superalloy components, there are a number of other factors affecting high temperature properties (γ′ precipitate size, grain size, oxygen content, etc.) of which the degree of grain twinning is only one.

3.3) Tensile Properties

Coarse, wide range & fine powders:

Tensile test results are shown in Figure 10. At room temperature (RT) the fine powder gave the highest tensile strength, as expected since it is well known that finer grains lead to higher tensile strength. The coarse powder had yield strength (YS) of 783 MPa, whilst the wide range was 800 MPa, and the fine powder was 815 MPa. Notably though, the coarse powder exhibited the highest ductility and better Ultimate Tensile Strength (UTS) than the wide range powder. This may be attributed to the fact that the coarse powder had good particle bonding with the least PPB precipitation and the highest degree of twinning in the microstructure. In the ET tests, however, there was slightly more variation in the properties between the powders. Tensile strength generally increased as the average powder particle size (and grain size) decreased. At 750°C, YS was 780 MPa for the coarse powder, 833 MPa for the wide range and 903 MPa for the fine. The tensile strengths achieved with all powders are comparable to cast CM247 material tested in [16-18]. Ductility in the as-HIP condition was

slightly better than the conventionally cast material, but lower than directionally solidified (DS) CM247LC reported by Kim *et al.* [16], though that may be expected due to the anisotropic nature of DS.

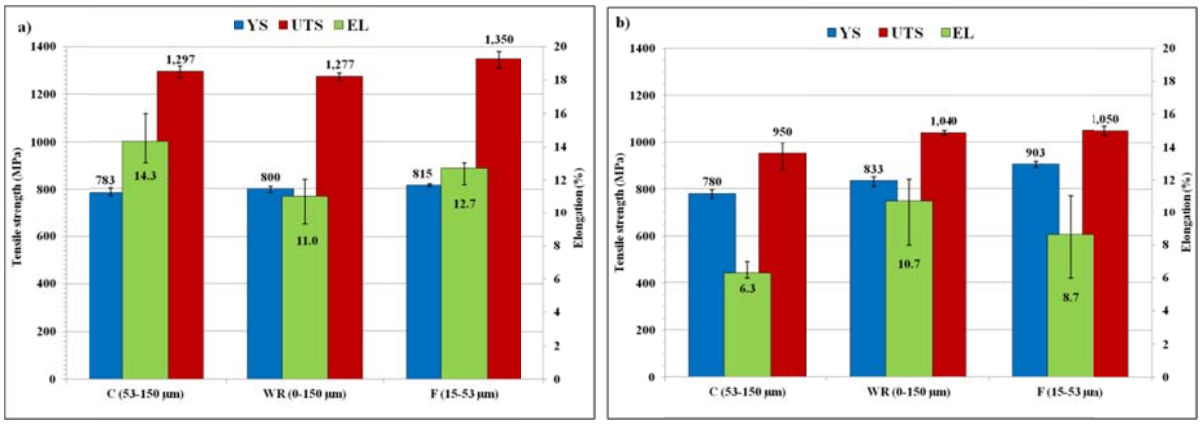

Figure 10: Tensile test results in the as-HIPped condition for all powders: (a) at room temperature (RT) the coarse powder gave the best balance of properties, (b) at elevated temperature (ET – 750°C) the wide range powder had the best balance of properties, while the coarse and fine powders exhibited a drop in hot ductility.

The promising properties of the coarse powder that were seen at RT were diminished at ET and particularly the hot ductility was affected, decreasing from 14% to 6% on average. All other factors being constant, it would be expected that the coarse powder would have maintained the best ductility at high temperature, due to it having the least PPB decoration and the highest degree of twinning, however, the drop in hot ductility may be explained by the fact that the coarse powder had lower boron content. Huron *et al.* [34] showed that there is an optimum B content, which is the most influential grain boundary element and affects various properties, so to give a good balance it should be at an intermediate level. It is thought that the B content of the coarse powder at only 20 ppm is too low whereas if that powder had around 140 ppm (similar to the wide range and fine powders), better ET tensile ductility may be expected. This again highlights that various factors affect properties and they must all be taken into account. The only other variable in that microstructure was the large, irregular HfO_2 inclusions, like those shown in figure 5(a), although it is unlikely they affected the hot ductility so considerably due to their sporadic/infrequent occurrence throughout the microstructure. The hot ductility of the fine powder also decreased at ET, from 13% to 9% although in this case the decrease was attributed to the higher degree of PPB decoration compared with the coarse powder. It can be seen from the clearly defined spherical particles

in the fracture surface in Figure 13(f) that this powder clearly exhibited the most particle debonding. The fracture surfaces for all powders consisted of a radial zone and shear lip zones. More ductile fracture surfaces, which exhibited few poorly bonded particles were seen when coarse powder particles were used, whereas such particles were common when the fine powder was used.

Sieved powders:

Results of the ET tensile tests on the sieved powders can be seen in Figure 11. Both sieved versions of the powder outperformed the WR powder. For the S_F powder, the hot ductility increase from 10.7% (WR) to 12.3%, suggesting the elimination of the very fine powder particles is beneficial. This can be attributed to reduction in the PPBs and carbide clusters, which are brought about by the very fine (<25 μm) powder particles. The hot ductility improved further with the S_C powder. This condition would be expected to perform the best due to the coarser powder particles, further promoting growth of recrystallised grains past the PPBs, as well as the higher fraction of Σ3 CSL boundaries. The Σ3 boundary fraction alone is clearly not the most dominant factor, since the S_F powder exhibited a higher Σ3 fraction than the S_C powder. In both cases the sieved powders exhibited comparable strength to cast CM247LC, however the ductility is higher than any equiaxed CM247LC reported in the literature and in the case of the S_C powder, almost as high as the ductility for conventional DS CM247LC reported by Kim *et al.* [16].

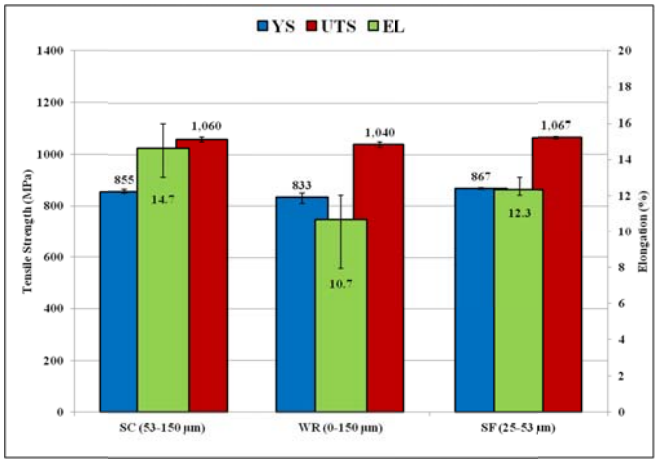

Figure 11: Tensile test results in the as-HIPped condition for the sieved versions of the wide range powder.

Care should be taken when assessing this data since there are various microstructural factors that can affect high temperature properties for Ni-superalloys. Alloy chemistry (e.g. O and B-contents), grain size and structure, strengthening precipitates, grain boundary character (e.g. twin boundaries), and the presence of defects can all also have an effect. The comparison of the powders from different suppliers showed that the nominal O-content of the powder can affect the formation of these twins, while the B-content can influence the ET properties. Furthermore, as evident by the sieved powders, the powder PSD (and its effect on O content) also influenced the formation of twin boundaries. The S_F powder exhibited higher Σ3 percentages than the S_C powder, but also a lower ductility (figure 12a). Another factor to consider is the tap density, since different PSDs lead to different tap densities, which can in turn affect the degree of recrystallisation during HIPping. Again however, there was no linear relationship between the tap density and the formation of Σ3 boundaries (figure 12b), although the WR exhibited both the lowest Σ3 fraction as the poorest ductility. It has been reported elsewhere [33], however, that the presence of multiple twinned clusters, known as twin related domains (TRDs) correlate to properties better than the actual length fraction of twin boundaries present. TRDs may contain multiple grains and twin chains, along with random grain boundaries. At triple points, the types of boundaries present (CSL or random) can determine if a crack will propagate or be suppressed. Therefore, although the Σ3 fraction has been used in the current work, the relationships shown in Figure 12 may be linear if TRDs were used as a measure against elongation. Further work would be needed to confirm this for the S_C and S_F powders. The study by Cortes *et al.* [32] on IN718 powder HIPping also reported a correlation between the Σ3 twin boundaries and the hot ductility, although in that case the HIP temperature was varied.

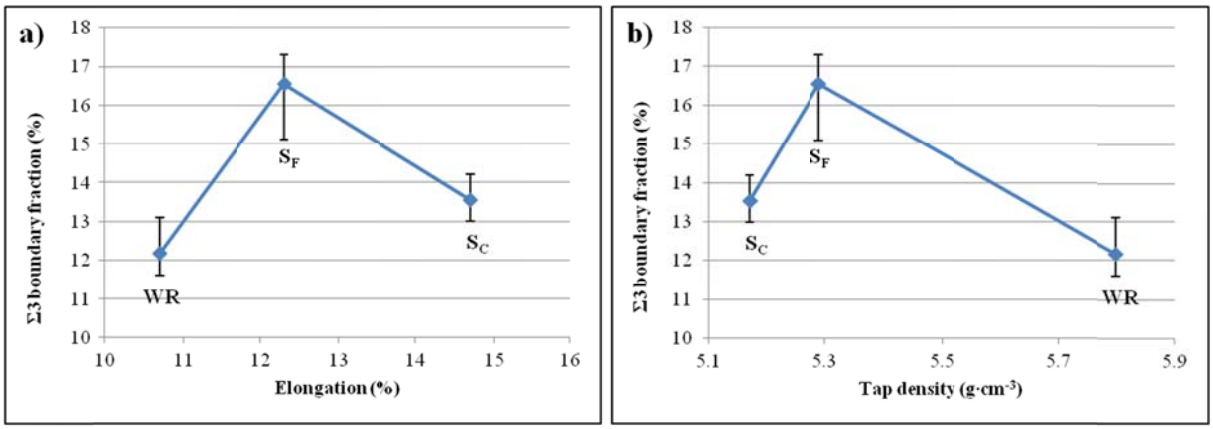

Figure 12: The variation of Σ3 boundary length fraction and associated ductility achieved between different PSDs for the WR powder and its sieved fractions S_F and S_C, showing (a) the

variation in elongation % and levels of Σ3 boundaries after HIPping, and (b) the variation in Σ3 levels boundaries and the powder tap density.

Comparison of the sieved and un-sieved powders:

The sieved powders in both PSDs outperformed the original 3 powders in the mechanical properties. For the coarse (C) powder, the poor hot ductility was attributed to the low B content and the presence of large, irregular HfO_2 inclusions in the microstructure (further study would be required to fully identify the contribution of each of these factors but it is likely they both contributed to the poor ductility to some extent). After sieving the WR powder to yield the S_C PSD, it was possible to achieve a (slightly) coarser microstructure promoting recrystallisation and grain growth with a powder containing higher B content (expected to provide strengthening) and the presence of only relatively small HfO_2 inclusions. Consequently, the hot ductility was not limited by the presence of defects hence more than doubled from 6.3 to 14.7%.

The S_F powder also exhibited higher hot ductility (12.3%) than the original fine (F) powder (8.7%). In this case, the B content of the WR powder and the fine powder were similar and the fine powder also exhibited finer HfO_2 inclusions in general. Therefore, the increase in ductility is attributed to a further reduction in PPB precipitation, despite the fact that there was not much difference between the PSDs. This may be attributed to the nominal O content of the original powders. The fine powder had 120ppm O, whereas the wide range powder had 75ppm O content (according to the supplier's data). After HIPping these increased to 240ppm and 140ppm as analysed using gas fusion, respectively. Within a given powder PSD, the O content would be expected to increase slightly if the coarse powder particles were removed (i.e. the 'fine' section of the WR powder may be expected to have higher O content than 140ppm due to the average particle size and the effect of surface area to volume ratio). However, the S_F PSD also had the sub-25 μm particles removed, which may have actually served to reduce the overall average O content. This would explain why the S_F powder exhibited a higher fraction of Σ3 boundaries than the WR powder. Therefore, it is also likely that after sieving, the S_F powder exhibited a lower O content than the un-sieved fine (F) powder.

3.4) Fractography

For the un-sieved powders, the RT and ET fracture surfaces appeared similar, so only the ET ones are included in Figure 13. The WR powder gave the best balance of properties at 750°C, which can be attributed to a combination of the various factors discussed. The WR powder had what is considered to be around the 'optimum' B content, unlike the C powder. Although the C powder exhibited a relatively ductile looking fracture mode (Figure 13b) some individual un-bonded particles could be found. Furthermore, the fracture surface was relatively flat (Figure 13a), with limited shear lips, suggesting a brittle fracture. Whilst there were no obvious signs of failure occurring at brittle HfO_2 inclusions in the current work, large irregular HfO_2 clusters were observed with this powder and have been reported elsewhere [11] as causing failure in mechanical test samples for HIPped CM247LC. For the WR powder, the B content was higher and HfO_2 inclusions were fewer, leading to much larger shear lips, Figure 13c. In figure 13d, the fracture surface appears generally ductile with evidence of micro-void coalescence and secondary cracking. For the F powder (which had similar B content to the WR), Figure 13f clearly shows failure along the PPBs, where numerous un-bonded, spherical powder particles can be seen. At RT, the effect of those factors (PPBs, HfO_2 inclusions and B content) may have been negligible since both the C and F powders gave a better average ductility than the WR. However, at 750°C, both had poorer ductility, whereas the WR retained on average a value around 11%, similar to its RT value.

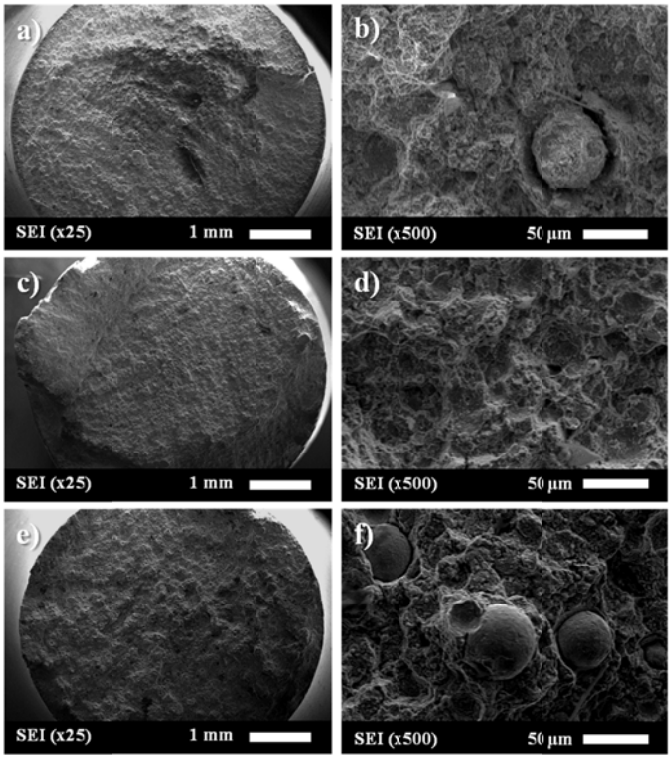

Figure 13: Fracture surfaces from the ET tensile tests showing (a & b) the coarse powder, (c & d) the wide range powder, and (e & f) the fine powder.

The fracture surfaces for the sieved powders are shown in Figure 14. For the S_C powder, large shear lips and relatively small radial zones were exhibited (Figure 14a) unlike the relatively flat fracture surface shown in Figure 13a for the un-sieved coarse powder. In Figure 14b, microvoid coalescence can be observed as well as flat facets, indicating the failure was clearly transgranular and did not occur along any defects. No poorly bonded powder particles where observed at all in these fracture surfaces.

When comparing the fracture surfaces of the original F powder, the sieved version (S_F) exhibited much more ductile fracture. Significant shear lips can be seen around the edge of the fracture surface in Figure 14c, whereas in figure 13e the fracture surface was much flatter. Figure 13f shows the previous sample clearly failed along PPBs, whereas the S_F powder did not show any unbonded powder particles in the fracture surface. Occasionally an individual particle could be distinguished, but generally they appeared deformed and well bonded. Microvoid coalescence and secondary cracking can be seen in figure 14d. When comparing the two fracture surfaces (figure 13f and 14b), the F powder clearly exhibits failure along the PPBs, showing numerous un-bonded powder particleswhich have retained their spherical shape. For the S_F powder, this was not the case, however, and no complete powder particles were observed in the fracture surfaces.

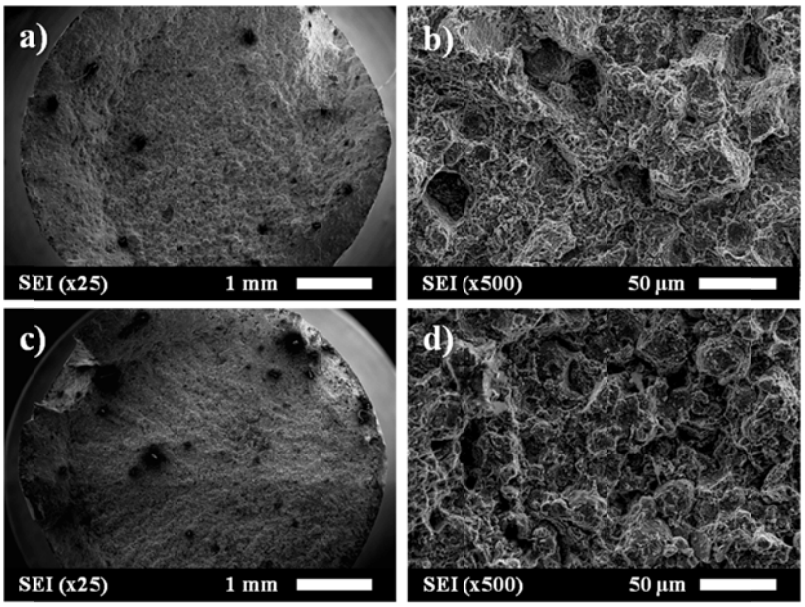

Figure 14: Fracture surfaces from the ET tensile tests for the sieved powders. The S_C powder (a,b) exhibited the best ductility in the current work resulting in (a) fracture surfaces with large shear lips ductile and (b) transgranular fracture. The S_F powder (c,d) exhibited (c) much bigger shear lips than the unsieved fine powder, and (d) much more ductile fracture surface showing microvoid coalescence and free from PPBs.

It is unlikely that the produced microstructures will be suitable for creep resistant structures due to the fine grain size and un-optimised γ′ structures, meaning that a post-HIP heat treatment is likely to be required, which is the subject of our next investigation. However, the HIPped-only material that was developed in this study can be applied in short-duration high temperature applications (e.g. stationary motorsport components) or in corrosive environments (e.g. oil and gas components) where superalloys are used. Post-HIP heat treatments are known to result in thermally induced porosity (TIPs), which is likely to undermine the fatigue behaviour of the material.

Conclusions

- Powder particle size was found to affect the grain size and PPB precipitation, with coarse powder particles (leading to lower O content in the HIPped material) encouraging grains to grow past the PPBs leaving carbide distributed throughout the microstructure.
- HfO_2 inclusions were found to be more of an issue with the coarse powder, although this can also be affected by the specific atomiser used in powder production.
- The particle size and O content appear to have affected the formation of twin boundaries, with an increased fraction of Σ3 boundaries achieved by using the coarse powder. Such boundaries are thought to be beneficial for high temperture properties. although they are only one of the various chemical and microstructural factors that control the properties.
- The best balance of high temperature properties was given by the wide range powder. It is thought that the low B content and the presence of coarse HfO_2 inclusions affected the hot ductility of the coarse powder, whilst PPB decoration affected the hot ductility of the fine powder.
- Tensile properties of the as-HIPped wide range powder were comparable to cast CM247LC at high temperature, with slightly lower strength but slightly better ductility.
- Sieving of the wide range powder into finer and coarser PSDs meant that the tensile properties were further improved over all of the the original powders including the parent wide-range PSD, by further elimination of PPB defects associated with the ultra-fine

powder particles, promoting further recrstallisation leading higher Σ3 boundary fractions and improvements in hot ductility.

Ackowledgements

The authors are grateful for financial support from the Engineering and Physical Sciences Research Council (EPSRC), UK and DSTL, UK through an ICase Award to JEM.

Data Availability

The raw/processed data required to reproduce these findings cannot be shared at this time due to technical or time limitations. EBSD raw data can be shared upon request.

References

1. Raisson, G., et al., *Production of net-shape static parts by direct HIPing of nickel base superalloy prealloyed powders.* Advanced Materials Research, 2011. **278**: p. 277-282.
2. Baccino, R., et al., *High performance and high complexity net shape parts for gas turbines: the ISOPREC® powder metallurgy process.* Materials & Design, 2000. **21**(4): p. 345-350.
3. Qui, C., *Net-shape hot isostatic pressing of a nickel-based powder superalloy*. PhD Dissertation, *Metallurgy & Materials*. 2010, University of Birmingham: UK.
4. Samarov, V., D. Seliverstov, and F.H. Froes, *18 - Fabrication of near-net-shape cost-effective titanium components by use of prealloyed powders and hot isostatic pressing*, in *Titanium Powder Metallurgy*, M.Q.H. Froes, Editor. 2015, Butterworth-Heinemann: Boston. p. 313-336.
5. Liu, H.-s., et al., *Effect of oxygen content and heat treatment on carbide precipitation behavior in PM Ni-base superalloys.* International Journal of Minerals, Metallurgy, and Materials, 2012. **19**(9): p. 827-835.
6. Rao, G.A., M. Srinivas, and D.S. Sarma, *Effect of oxygen content of powder on microstructure and mechanical properties of hot isostatically pressed superalloy Inconel 718.* Materials Science and Engineering: A, 2006. **435–436**(0): p. 84-99.
7. Jablonski, D.A., *The effect of ceramic inclusions on the low cycle fatigue life of low carbon astroloy subjected to hot isostatic pressing.* Materials Science and Engineering, 1981. **48**(2): p. 189-198.
8. Qiu, C.L., et al., *Influence of hot isostatic pressing temperature on microstructure and tensile properties of a nickel-based superalloy powder.* Materials Science and Engineering: A, 2013. **564**(0): p. 176-185.
9. Pollock, T.M. and S. Tin, *Nickel-based superalloys for advanced turbine engines: Chemistry, microstructure, and properties.* Journal of Propulsion and Power, 2006. **22**(2): p. 361-374.
10. Rao, G.A., M. Srinivas, and D.S. Sarma, *Influence of modified processing on structure and properties of hot isostatically pressed superalloy Inconel 718.* Materials Science and Engineering: A, 2006. **418**(1–2): p. 282-291.
11. Zhang, Q., *The microstructures and properties of powder HIPped nickel-based superalloy CM247LC*. PhD Dissertation, *Metallurgy & Materials*. 2011, University of Birmingham: UK.
12. Zhang, L., et al., *Thermal evolution behavior of carbides and γ' precipitates in FGH96 superalloy powder.* Materials Characterization, 2012. **67**(0): p. 52-64.
13. Seiser, B., R. Drautz, and D.G. Pettifor, *TCP phase predictions in Ni-based superalloys: Structure maps revisited.* Acta Materialia, 2011. **59**(2): p. 749-763.
14. Wu, K., et al., *Alloy Design of a New Type High-Performance P/M Turbine Disk Superalloy*. Procedia Engineering, 2012. **27**(0): p. 939-953.

15. Kong, Y.H. and Q.Z. Chen, *Effect of minor additions on the formation of TCP phases in modified RR2086 SX superalloys.* Materials Science and Engineering: A, 2004. **366**(1): p. 135-143.

16. Kim, I.S., et al., *Influence of heat treatment on microstructure and tensile properties of conventionally cast and directionally solidified superalloy CM247LC.* Materials Letters, 2008. **62**(6–7): p. 1110-1113.

17. Huang, H.-E. and C.-H. Koo, *Characteristics and Mechanical Properties of Polycrystalline CM 247 LC Superalloy Casting.* Materials Transactions, 2004. **45**(2): p. 562-568.

18. Huang, H.-E. and C.-H. Koo, *Effect of Solution-Treatment on Microstructure and Mechanical Properties of Cast Fine-Grain CM 247 LC Superalloy.* Materials Transactions, 2004. **45**(4): p. 1360-1366.

19. Harris, K., G. Erickson, and R. Schwer. *MAR-M247 derivations—CM247 LC DS alloy, CMSX single crystal alloys, properties and performance*. in *5th Int. Symp*. 1984.

20. Zhang, J. and R.F. Singer, *Hot tearing of nickel-based superalloys during directional solidification.* Acta Materialia, 2002. **50**(7): p. 1869-1879.

21. Carter, L.N., *Selective laser melting of nickel superalloys for high temperature applications*. PhD Dissertation, *Metallurgy and Materials*, 2013, University of Birmingham, UK.

22. Kendall, J.M., et al., *Microstructural Design for Fatigue Crack Growth Resistance in Ni-base Alloy*. 1989: Rolls-Royce plc.

23. Jackson, M. and R. Reed, *Heat treatment of UDIMET 720Li: the effect of microstructure on properties.* Materials Science and Engineering: A, 1999. **259**(1): p. 85-97.

24. May, J.R., et al., *Microstructure and Mechanical Properties of an Advanced Nickel-Based Superalloy in the as-HIP Form.* Advanced Materials Research, 2011. **278**: p. 265-270.

25. Mitchell, R.J., H.Y. Li, and Z.W. Huang, *On the formation of serrated grain boundaries and fan type structures in an advanced polycrystalline nickel-base superalloy.* Journal of Materials Processing Technology, 2009. **209**(2): p. 1011-1017.

26. Koul, A.K. and G.H. Gessinger, *On the mechanism of serrated grain boundary formation in Ni-based superalloys.* Acta Metallurgica, 1983. **31**(7): p. 1061-1069.

27. Loyer, H.D., M.; Macia, T;, Sanders T. H., Khan, T, *Mechanisms of formation of serrated grain boundaries in nickel base superalloys.* Superalloys, 1996: p. 119-127.

28. Qiu, C.L. and P. Andrews, *On the formation of irregular-shaped gamma prime and serrated grain boundaries in a nickel-based superalloy during continuous cooling.* Materials Characterization, 2013. **76**(0): p. 28-34.

29. Yeh, A.-C., et al., *Effect of serrated grain boundaries on the creep property of Inconel 718 superalloy.* Materials Science and Engineering: A, 2011. **530**(0): p. 525-529.

30. Detrois, M., et al., *Grain boundary engineering of powder processed Ni-base superalloy RR1000: Influence of the deformation parameters.* Materials Science and Engineering: A, 2015. **627**: p. 95-105.

31. Marrow, J., et al., *Grain boundary control for improved intergranular stress corrosion cracking resistance in austenitic stainless steels: new approach.* Energy Materials, 2006. **1**(2): p. 98-102.

32. Cortes, J., et al., *Effect of HIP temperature and post-HIP heat treatments on coincidence site lattices and twin boundaries in IN718*. EPMA Conference, Hamburg, October 2016.

33. Irukuvarghula, S., et al., *Evolution of grain boundary network topology in 316L austenitic stainless steel during powder hot isostatic pressing.* Acta Materialia, 2017. **133**: p. 269-281.

34. Huron, E.S., et al., *The influence of grain boundary elements on properties and microstructures of P/M nickel base superalloys.* Superalloys 2004, 2004: p. 73–82.